



The dual role of shot peening in hydrogen-assisted cracking of PSB1080 high strength steel



Xinfeng Li ^a, Jin Zhang ^b, Yanfei Wang ^c, Mingming Ma ^d, Sicong Shen ^a, Xiaolong Song ^{a,*}

^a State Key Laboratory for Mechanical Behavior of Materials, School of Materials Science and Engineering, Xi'an Jiaotong University, Xi'an 710049, China

^b Department of Geosciences, Center for Materials by Design, and Institute for Advanced Computational Science, State University of New York, Stony Brook, NY 11794-2100, USA

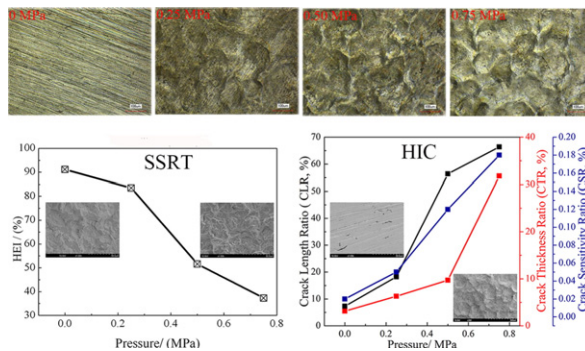
^c School of Chemical Engineering & Technology, China University of Mining and Technology, Xuzhou 221116, China

^d School of Department of Heat Treatment and Surface Treatment, Avic Aircraft Co., Ltd. Xi'an Brake Branch, Xingping 713106, China

HIGHLIGHTS

- With increasing in SP pressure, the hydrogen diffusion coefficient decreases.
- SP delays the onset of intergranular fracture.
- For reversible hydrogen embrittlement, the resistance to hydrogen embrittlement increases as the SP pressure increases.
- For irreversible hydrogen embrittlement, the resistance to HIC decreases as SP pressure increases.

GRAPHICAL ABSTRACT



ARTICLE INFO

Article history:

Received 19 May 2016

Received in revised form 24 July 2016

Accepted 25 July 2016

Available online 27 July 2016

Keywords:

High strength steel

Hydrogen-assisted cracking

Shot peening

Residual stress

ABSTRACT

The influence of shot peening (SP) treatment on reversible and irreversible hydrogen embrittlement of PSB1080 steel was investigated using slow strain rate tensile tests and electrochemical hydrogen charging-induced cracking tests, respectively. The results demonstrate that SP plays the dual role in hydrogen-assisted cracking. On the one hand, the resistance to hydrogen embrittlement increases as the SP pressure increases for reversible hydrogen embrittlement. This is ascribed to the fact that the shot peening layer acts as a barrier from hydrogen invasion, which is illustrated by hydrogen permeation tests and fracture surface observation. On the other hand, the susceptibility to hydrogen-induced cracking increases with an increase in SP pressure for irreversible hydrogen embrittlement. The crack initiation is associated with inclusions rich in O, Fe, Al and Si or in O, Fe, Si and S for no shot peening sample, while for SP specimen both inclusions and crater rim serve as crack origins. In addition, the hydrogen-induced crack path exhibits a long strip shape for no shot peening sample, whereas the branch-type cracks are observed in SP specimens.

© 2016 Elsevier Ltd. All rights reserved.

1. Introduction

Due to good durability performance, prestressed concrete structures have been widely used in infrastructures, such as bridges and nuclear power plants. High strength steel bars are attractive materials for the structures as they can bond well with the concrete and withstand

* Corresponding author.

E-mail address: songxl@mail.xjtu.edu.cn (X. Song).

most of the tensile stress acting on the structure. In general, the steel bars are immune to corrosion due to two reasons. One is that the concrete is a physical barrier to the ingress of aggressive substances to the steel bars. The other is that the solution filling the concrete pores is alkaline, around PH 12.6, thus keeps the steel in a passive condition [1,2].

Unfortunately, despite these protections, external aggressive agents can still invade into the structures and come in contact with the surfaces of the steel bars, induce the breakdown of the passive layers and then lead to the initiation and growth of local pitting corrosion. Once the pitting corrosion emerges with the acid environment, hydrogen atoms can be generated through the following cathodic partial reaction: $H^+ + -e^- \rightarrow H_{at}$ [3,4]. It has well-established that hydrogen can degrade many steels' mechanical properties, such as ductility and cracking resistance. This is known as hydrogen embrittlement or hydrogen-induced cracking. Therefore, as the hydrogen atoms generated in the corrosion pits absorb the surface of the steel and diffuse into the interior of the steel, the steel bars are very likely to be degraded in the presence of hydrogen. In fact, many premature failures cases of the pre-stressed steel bars have been reported, and the cause of the failures are attributed to hydrogen embrittlement [2,5].

Hydrogen can cause embrittlement of steels, which is divided into reversible and irreversible hydrogen embrittlement [6]. In the case of reversible embrittlement, atomic hydrogen interacts with defects, such as vacancies, dislocations and grain boundaries. However, ductility can be restored to the steel as a result of desorption of dissolved hydrogen, particularly at elevated temperature. In the case of irreversible hydrogen embrittlement, the association of atomic hydrogen species inside the iron crystal may lead to the formation of H_2 in special sites, such as inclusion sites, according to the equilibrium $2[H](\text{atomic hydrogen}) \rightarrow H_2(\text{gas})$ [7,8]. The high pressure of gaseous hydrogen may cause the deformation of surrounding metallic matrix or even cracking. Electrochemical hydrogen charging test is an advanced method that provides useful information on hydrogen embrittlement susceptibility of metallic materials, and can be applied to evaluate reversible hydrogen embrittlement [9,10] and irreversible hydrogen embrittlement [11–13].

Shot peening (SP) technology, as a mechanical surface modification technique, can induce compressive residual stress and lead to the formation of substructure in the surface layer. It can be used to improve the fatigue durability [14], corrosion resistance [15], stress corrosion cracking [16] of metal materials. The effect of peening treatment on hydrogen embrittlement of various metallic materials has been studied and the results are controversial. Bockris et al. [17] and Wilde et al. [18] revealed that the plastic deformation and compressive stress in iron and steel suppressed hydrogen permeability effectively, and suggested SP as a potential approach to combatting hydrogen-induced fracture in steel. Ma et al. [19] demonstrated that hydrogen embrittlement of intermetallics $Ni_3(Si, Ti)$ in a moisture air or an aqueous solution was reduced at room temperature after SP treatment. Takakuwa et al. suggested that the compressive residual stress introduced by cavitation peening suppressed the invasion of hydrogen into the 316 L austenite stainless steel [20], and found that the crack propagation rate of hydrogen charging samples was suppressed by 75% after cavitation peening [20]. However, Verpoort et al. [21] reported that SP of nickel increased high cycle fatigue life, but reduced low cycle fatigue life in the presence of hydrogen atmosphere or precharged specimens. Brass et al. [22] suggested that for low-carbon steel SP reduced the susceptibility to hydrogen embrittlement in precharged specimen, whereas increased hydrogen embrittlement in a severe hydrogen environment (H_2S). For 304 stainless steel, SP increased hydrogen embrittlement due to the phase transformation from γ to α'' . In addition, Marchi et al. [23] revealed that laser peening enhanced the hydrogen-assisted fracture of Alloy 22.

At present, the effect of SP treatment on hydrogen embrittlement of high strength steels has not been well investigated. Thus, this paper aims to study the effect of SP on hydrogen diffusion behaviors and hydrogen embrittlement of PSB1080 high strength steel using hydrogen

permeation tests, slow strain rate tensile (SSRT) tests and electrochemical hydrogen charging-induced cracking (HIC) tests, respectively. The susceptibility to hydrogen embrittlement at various SP pressures is evaluated and analyzed. In addition, crack initiation and propagation mechanism of no shot peening (un-SP) and SP samples are determined.

2. Experimental procedures

2.1. Sample preparation

Screw-thread high strength steel bars PSB1080 with a chemical composition of 0.27C–1.55Si–2.20Mn–0.011P–0.0043S–0.97Cr–0.007Ni–0.017Cu–0.008Al–Fe (all in wt.%) were used. The steel bars were subjected to following heat treatment. Size 150 mm × 150 mm steel billets were hot-rolled to a diameter of 40 mm steel bars, air-cooled to room temperature and then tempered at 350 °C for 5 h. The mechanical properties of PSB1080 steel are listed in Table 1. The SSRT, HIC and hydrogen permeation specimens were machined along the longitudinal direction of the bars. The dimensions of SSRT specimens and HIC or hydrogen permeation test specimens are shown in Fig. 1(a) and (b), respectively.

All specimens were ground with different grades SiC paper from 80 to 800 and then cleaned in deionised water. Ultrasonic cleaning was also used to degrease the sample surface in ethanol. Subsequently, the specimens were subjected to SP treatment.

2.2. SP treatment

SP treatment was performed with an injector type machine using different SP pressures at 0.25 MPa, 0.50 MPa, 0.75 MPa, respectively. Cast steel balls with a diameter of 250 μm were used. The distance between the nozzle and samples was 50 mm and duration of peening time was 60 s, as listed in Table 2.

The specimens for SSRT, HIC and hydrogen permeation tests were divided into four groups. One group was directly machined without SP treatment while other three groups were treated by SP at various pressures. For SSRT tests, the gauge parts (the dot pattern area shown in Fig. 1(a)) of the three groups specimens were subjected to SP treatment with three peening's pressures of 0.25 MPa, 0.50 MPa and 0.75 MPa, respectively. In order to generate homogeneous SP layers on the surface of samples, the specimens were rotated during SP treatment. Moreover, the professional plastic hollow pipe with a thickness of 1 mm was mounted on the threaded part of samples to avoid SP treatment. For hydrogen permeation and HIC samples, both surfaces were treated by SP, as indicated in Fig. 1(b). Previous study [22,24,25] has revealed that a more typical approach for studying hydrogen permeability through a surface layer into the bulk material is by using only one-side treated specimens. However, in the present study the specimens for the hydrogen permeability tests treated by SP from both sides were selected, which were attributed to three reasons. Firstly, previous study investigates tritium (isotope of hydrogen) permeability using two sides treated samples. Reiter et al. [26] studied the barriers impact on the tritium permeation in the Li17-Pb blanket with no coating, a coating on the Li17-Pb side only and for coatings on all surfaces. Secondly, hydrogen permeation behaviors depend on the direction of sample's peening side during hydrogen permeation tests. Brass and Chene [22] reported that shot peening did not induce any change in the diffusivity for a low-carbon steel when the peened side of the sample was faced the cathodic compartment of cell. However, when permeation tests were conducted with the peened side facing the detection compartment of the

Table 1
Mechanical properties of PSB1080 steel.

	Yield strength/MPa	Tensile strength/MPa	Reduction of area/%	Elongation at fracture/%	Hardness/HV
PSB1080	1276.11	1432.96	62.04	15.61	~530

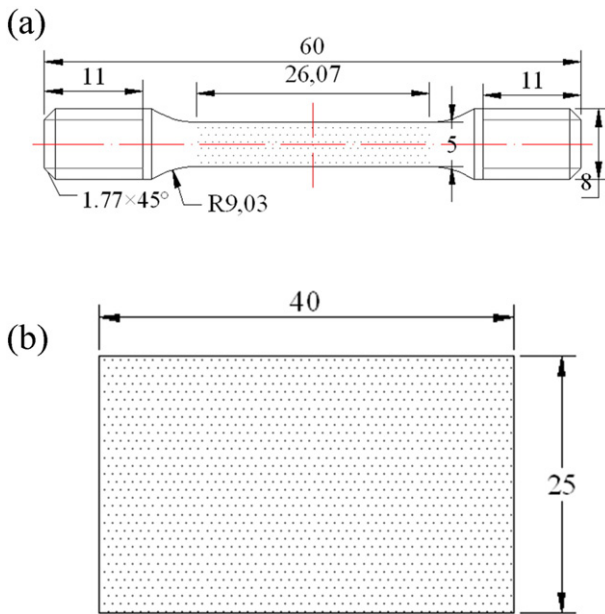


Fig. 1. (a) Dimensions of the specimen used in the SSRT tests and (b) dimensions of hydrogen permeation tests or hydrogen-induced cracking tests specimens with a thickness of 0.88 mm. Note 1: all dimensions shown in millimeters (mm). Note 2: dot pattern indicated shot peening treatment area.

cell, the shot peening layer can induce a large decrease in hydrogen diffusivity. After SP treatment on both sides of sample, the dependence of hydrogen permeation results on the direction of sample's peening surface was eliminated. Thirdly, HIC tests were conducted on the SP samples from both sides. In order to be consistent with HIC samples, the samples for hydrogen permeation tests were subjected to SP treatment on both sides.

2.3. Materials characterization

The microstructure of the alloy was observed by optical microscopy (OM), scanning electron microscopy (SEM) and transmission electron microscopy (TEM). The sample preparation process had been detailedly described in the previous reference [11]. To reveal the morphological characteristics of un-SP and SP samples, 3D laser scanning confocal microscope was used offering a 1 nm resolution.

The surface residual stress introduced by the SP was determined by the $\sin[2]\psi$ method [27] using Rigaku MSF/PSF-3M X-ray stress analyzer with a Cr target operated at 30 kV and 6 mA. X-ray from $K\alpha$ peak with spot size $1 \times 1 \text{ mm}^2$ was chosen. The diffractive angle 2θ was varied from 141.92° to 168.48° using a scintillation counter at angle of $\psi = 0, 18.4, 26.6, 33.2, 39.2$ and 45.0° . The diffractive plane was the (211) plane of α -Fe. The diffractive angle without strain 2θ was 156.00° , and the stress constant was $-318.0 \text{ MPa deg}^{-1}$. In-depth measurement of residual stress was carried out by using chemical corrosion method. A solution of aqua regia, which consisted of hydrochloric acid and nitric acid fuming with the volume ratio 3:1, was used to thin the specimens. In order to determine the hardness distribution on the cross section of

the specimens, microhardness tests were performed using the micro Vickers hardness tester with a load of 0.98 N and a dwell time of 10 s.

2.4. Hydrogen permeation tests

The hydrogen permeation device was composed of an electrolytic cell with two compartments (cathodic and anodic sides), a reference electrode ($Hg/HgO/NaOH$ 0.1 M NaOH), two auxiliary electrodes (Pt plate) and two potentiostat/galvanostat. The specimen with an exposed surface area of 2.27 cm^2 on each side was mounted between the compartments. One side of the specimen acted as hydrogen entry side. It was galvanostatically polarized at a constant charging current density (20 mA cm^{-2}) in $0.5 \text{ mol L}^{-1} \text{ H}_2\text{SO}_4$ with $0.824 \text{ g L}^{-1} \text{ Na}_4\text{P}_2\text{O}_7$. The hydrogen exit side of the cell was potentiostatically maintained at a constant potential of 0.2 V versus reference electrode.

The steady-state hydrogen permeation flux $J_\infty (\text{mol m}^{-2} \text{ s}^{-1})$ was calculated according to following equation [11,28]:

$$J_\infty = \frac{I_p^\infty}{nF}. \quad (1)$$

The apparent hydrogen diffusivity $D_{app} (\text{m}^2 \text{ s}^{-1})$ was determined by the break-through method as:

$$D_{app} = \frac{L^2}{6t_L}. \quad (2)$$

If the charging surface was in equilibrium, the apparent subsurface concentration $C_{app} (\text{mol m}^{-3})$ can be calculated by:

$$C_{app} = \frac{J_\infty L}{D_{app}}. \quad (3)$$

In the equations listed above, n was the number of electrons transferred, $F (\text{C mol}^{-1})$ was the Faraday's constant, $L (\text{m})$ was the specimen thickness, $t_L (\text{s})$ was the lag time, defined as 0.63 times the steady-state value.

2.5. SSRT test

Prior to SSRT tests, hydrogen was introduced into the specimens without or with SP by electrochemical hydrogen charging in a $0.5 \text{ mol L}^{-1} \text{ NaOH}$ solution at a constant cathodic current density of 3 mA cm^{-2} for 24 h. This hydrogen charging solution can generate mild condition, i.e., the content of hydrogen invasion is low. Moreover, to prevent hydrogen releasing from the pre-charged specimens, cadmium electroplating was immediately carried out after hydrogen-charging in accordance with our previous method [29].

The SSRT experiments were immediately conducted within 5 min after cadmium electroplating using an universal tensile testing machine 1195 in accordance with ASTM E8M-2009. The tensile rate was at a crosshead speed 0.03 mm min^{-1} , corresponding to a normal strain rate of $2 \times 10^{-5} \text{ s}^{-1}$. The index of relative susceptibility to hydrogen embrittlement of specimens was determined by measuring the relative loss in reduction of area, which can be expressed as:

$$\text{HEI} = \frac{\varphi_0 - \varphi_H}{\varphi_0} \times 100\% \quad (4)$$

where φ_0 and φ_H were the reduction of area of hydrogen-free and hydrogen-charged specimens, respectively.

After SSRT tests, fracture surfaces of samples were analyzed using SU6600 field emission scanning electron microscopy.

Table 2
Parameters of shot peening treatment.

Peening media	Size of media (μm)	Distance between nozzle and specimen (mm)	Peening pressure (MPa)	Peening's time (s)	Coverage
Cast steel balls	250	50	0.25 0.5 0.75	60	100%

2.6. HIC test

The specimens for HIC tests were hydrogen-charged in 0.5 mol L⁻¹ H₂SO₄ solution at a constant current density of 20 mA cm⁻² for 1 h. The CH₄N₂S (1 g L⁻¹) was added in the solution as a hydrogen recombination poison. This case induced aggressive conditions that can introduce hydrogen-induced cracks. In comparison with NaOH solution, H₂SO₄ solution contained more H⁺ ions, which promoted hydrogen invasion into the steel. The addition of CH₄N₂S suppressed the formation of hydrogen molecules, further accelerating hydrogen entry. In addition, platinum sheet was used as an anode and the specimen was used as a cathode during hydrogen charging. After the tests, the three polished metallographic sections of each sample were inspected for cracks. The HIC susceptibility indexes of crack length ratio (CLR), crack thickness ratio (CTR) and crack sensitivity ratio (CSR) for each sample were calculated in accordance with NACE standard TM0284-2003:

$$\text{Crack Length Ratio : CLR} = \frac{\sum a}{W} \times 100\% \quad (5)$$

$$\text{Crack Thickness Ratio : CTR} = \frac{\sum b}{T} \times 100\% \quad (6)$$

$$\text{CrackSensitivityRatio : CSR} = \frac{\sum (a \times b)}{W \times T} \times 100\% \quad (7)$$

where *a* was the crack length, mm, *b* was the crack thickness, mm; *W* was the section width, mm; *T* was the test specimen thickness, mm.

In addition, crack initiation and propagation of the HIC specimens were also examined by SEM. To determine the chemical composition of inclusions in the steel, energy dispersive spectroscopy (EDS) was used.

3. Results

3.1. Microstructure and inclusions

The microstructure of the PSB1080 steel consists of martensite (M) and granular banite (GB), as shown in Fig. 2(a). The prior austenite grain is about 13 μm in size. Fig. 2(b) shows the inclusions, which are one of the dominant factors affecting the hydrogen-assisted cracking. The inclusions are present in spherical shape and have a relatively uniform distribution. Fig. 2(c)–(d) show the cross sectional microscopic observation of samples after etching. In comparison with un-SP sample (Fig. 2(c)), the plastically deformed region on the surface layer (the dark region indicated in Fig. 2(d)) is formed in 0.50 MPa SP sample. Moreover, TEM images of surface layer in un-SP and SP (0.50 MPa) specimens are also present in Fig. 2(e) and (f), respectively. Un-SP specimen exhibits lath martensite with the spacing of lath about 190 nm, while the pattern of lath martensite almost disappears and a large amount of dislocations form at the interior or lath boundaries of martensite in the SP specimen, indicating that SP increases dislocation density.

3.2. Surface morphology

The surface morphology of the alloy without and with SP is shown in Fig. 3. For un-SP sample, the surface morphology is relatively flat with remaining parallel scratches, as shown in Fig. 3(a)–(aa). In contrast, the surface features of SP samples exhibits a number of craters, overlaps between the craters, and no microcracks are observed. The quantity results given by surface roughness measurements (arithmetical mean roughness (Ra) and maximum height of the profile (Rz)) are shown in Fig. 4. With an increase in SP pressure, the surface roughness increases significantly. The value of Ra for 0.75 MPa SP sample is 2.941 μm, which is twice higher than that of un-SP specimen (1.003 μm). Rz of un-SP and 0.75 MPa SP samples is 11.681 μm and 18.718 μm, respectively.

3.3. Residual stress and microhardness

The microhardness-depth profiles are illustrated in Fig. 5(a). Since SP induces plastic deformation, there is a conspicuous increase in microhardness in the near-surface region. The depth of plastic deformation layer can be roughly estimated in the range of 250–350 μm.

Fig. 5(b) demonstrates the relationship between residual stress and depth, implying that SP induces compressive residual stress. As SP pressure enhances, compressive residual stress increases under the same depth. In addition, the maximum compressive residual stress of un-SP specimen is located on the specimen surface, while it moves towards the interior for SP specimens. This is attributed to the fact that the residual stress may partially be relaxed by the surface defects, such as craters overlap [30].

3.4. SSRT test

Stress-displacement curves of hydrogen-free and hydrogen-charged specimens subjected to un-SP and SP treatment are shown in Fig. 6. Regardless of SP or not, tensile stress increases, reaches the peak value and then decreases with an increase in displacement for all hydrogen-free samples. However, the fracture displacement for all hydrogen-charged samples decreases in comparison with that of hydrogen-free specimens, especially for un-SP sample that premature failure occurs at the end of elastic stage. In addition, the degree of necking increases as the SP pressure increases. The relationship between mechanical properties for hydrogen-free and hydrogen-charged specimens and SP pressure are given in Fig. 7. Under the same SP pressure, hydrogen charging slightly decreases the tensile strength (Fig. 7(a)) and reduces significantly both elongation and reduction of area, especially in un-SP specimens, as shown in Fig. 7(b) and (c). Moreover, HEI decreases with an increase in SP pressure, implying that SP treatment increases the resistance to hydrogen embrittlement. In addition, the hydrogen-charged un-SP sample and 0.75 MPa SP sample were tempered at 200 °C for 1 h and then tensioned. The ductility of both samples almost recovers, as shown in Fig. 8. Thus, it is designated as reversible hydrogen embrittlement.

Fig. 9 exhibits SEM fractographs of hydrogen-free specimens, indicating plastic fracture with a cup and cone fracture regardless of shot peening or not, as shown in Fig. 9(a) and (c). High magnification images of both un-SP and SP (0.75 MPa) specimens exhibit dimple fracture mode, as shown in Fig. 9(b) and (d), respectively. For hydrogen-charged specimens, the macro-fracture appearance of un-SP sample shows brittle fracture (Fig. 10(a)) and high magnification image presents a mixed fracture features: intergranular fracture (IG) and quasi-cleavage fracture (QC), while a little necking on the macro-fracture surface can be observed in the SP (0.75 MPa) specimen, as shown in Fig. 10(c). The fracture characteristics are mainly quasi-cleavage fracture with some dimple fracture, as shown in Fig. 10(d), revealing that SP suppresses the onset of intergranular fracture.

3.5. HIC observation

3.5.1. Overviews of hydrogen-induced cracks

Fig. 11 gives typical surface hydrogen-induced cracks, which is designated as irreversible hydrogen embrittlement, at different SP pressure samples after HIC tests. It can be seen that the crack is a long strip shape (indicated by black arrows in Fig. 11(a)) with the maximum length about 16 μm and a small circle shape (indicated by red arrows in Fig. 11(a)) with a diameter about 2.4 μm for un-SP specimen. This result is in accordance with the references [31,32]. However, the branch-type cracks are observed in all SP specimens and there are some specific cracks, which maybe serve as crack origin, mainly walking along the crater rims, as indicated by red ellipses in Fig. 11(b), (c) and (d), at the end of which more than two cracks take place. In addition, the approximately peak crack length for 0.25 MPa, 0.50 MPa and 0.75 MPa SP specimens is 261 μm, 302 μm and 637 μm, respectively. Fig. 12 shows the maximum

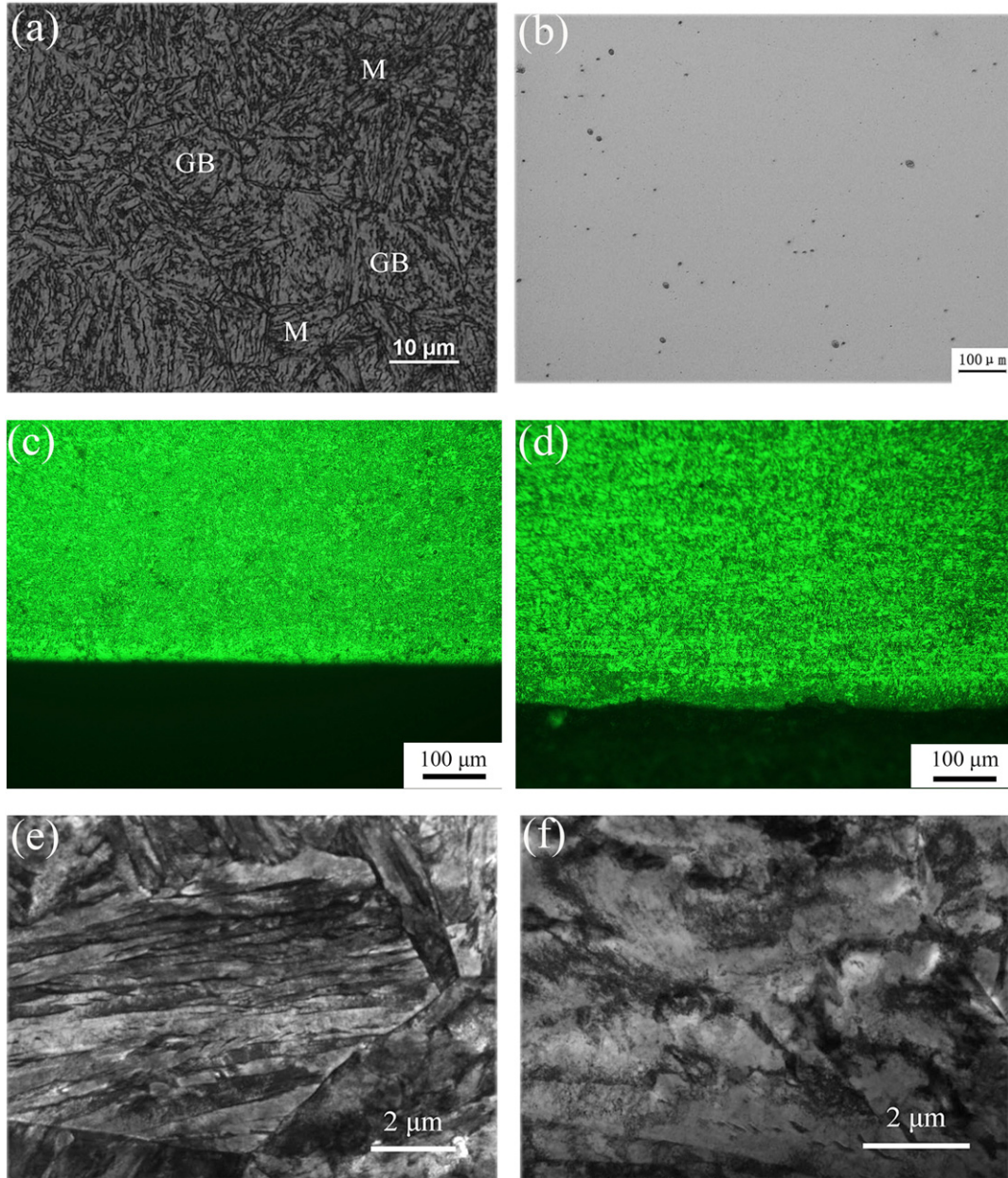


Fig. 2. (a) Optical micrograph; (b) inclusions; cross sectional micrograph (c) 0 MPa sample, (d) 0.50 MPa sample; TEM micrograph of surface layer (e) 0 MPa sample; (f) 0.50 MPa sample.

crack along transversal section at various SP pressures after HIC tests. For un-SP sample, there is no macroscopic crack beneath the surface, as shown in Fig. 12(a), whereas the SP specimens exhibit different size cracks. As SP pressure increase, both the crack length and the crack depth from the surface increase, as shown in Fig. 12(b)–(d).

The values of CLR, CTR and CSR for different SP pressures are shown in Fig. 13. As the SP pressure increases, all of them increase, indicating that the resistance to HIC decreases due to SP treatment.

3.5.2. HIC cracks initiation and propagation

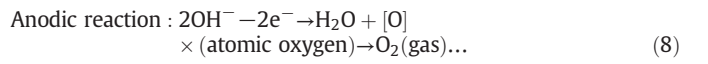
For un-SP specimen, the cracks initiate at the inclusions and the composition of inclusions are enriched in O, Fe, Al and Si (marked as A) or in O, Fe, Si and S (marked as B), as shown in Fig. 14. While two types of cracks initiation sites are observed in SP sample (0.75 MPa), one type of the crack is associated with inclusion rich in O and Si, as shown in Fig. 15(a) and (b), and the other is located along the crater rim, as shown in Fig. 15(c). Moreover, the crack propagation path is either along the crater rim, as shown in Fig. 15(d), or a typical stepwise crack [32,33], as shown

in Fig. 15(e). Further, the surface layer of 0.75 MPa SP sample subjected to HIC test was ground, mechanically polished and etched. It can be seen that hydrogen-induced cracks are dominantly transgranular fracture with some intergranular fracture, as shown in Fig. 16.

4. Discussion

4.1. Effect of SP treatment on reversible hydrogen embrittlement

The accepted reactions of steel surface during electrochemical hydrogen charging are:



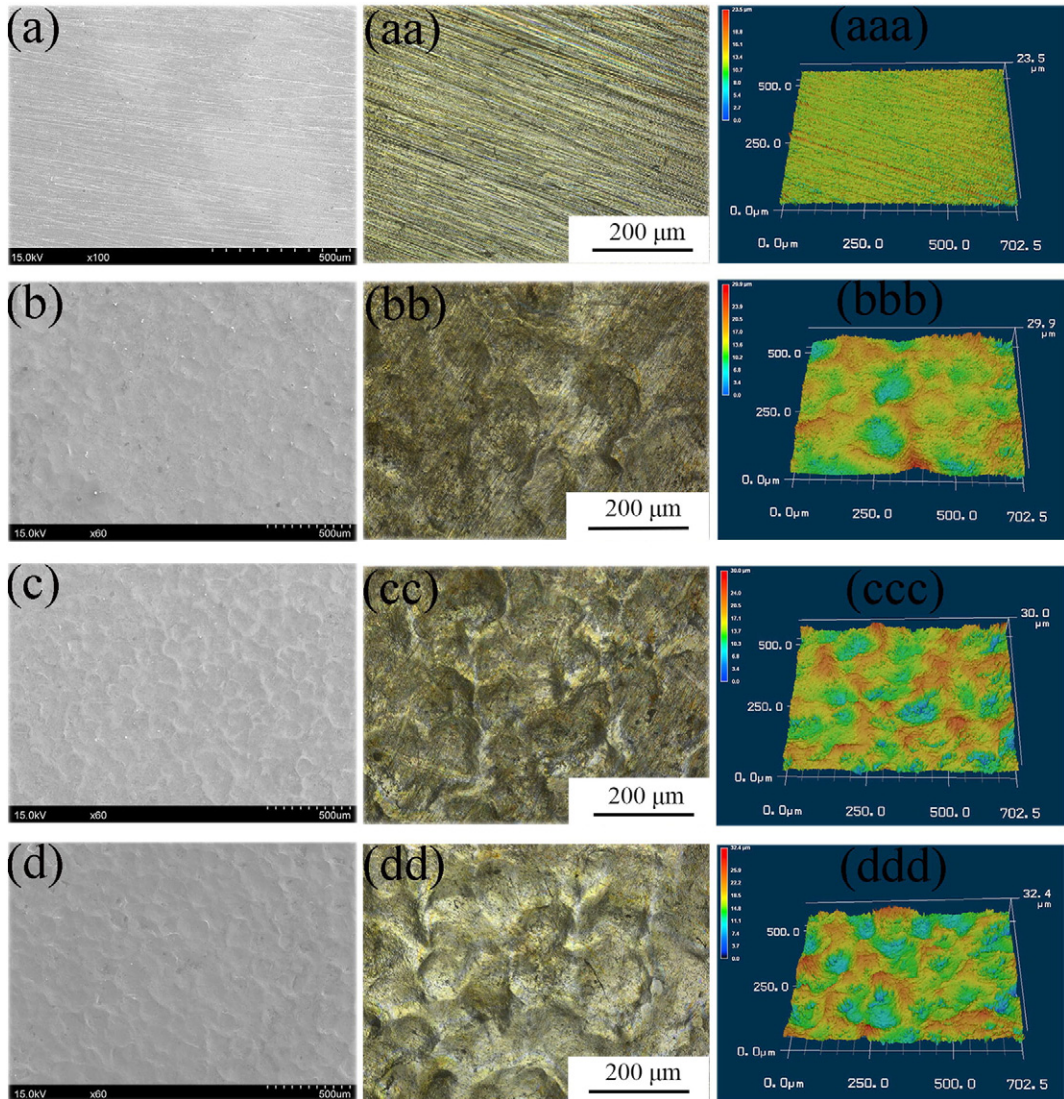


Fig. 3. Surface morphology of samples with or without shot peening. (a), (aa) and (aaa) showing no shot peening sample; (b), (bb) and (bbb) showing 0.25 MPa SP sample; (c), (cc) and (ccc) showing 0.50 MPa SP sample; (d), (dd) and (ddd) showing 0.75 MPa SP sample.

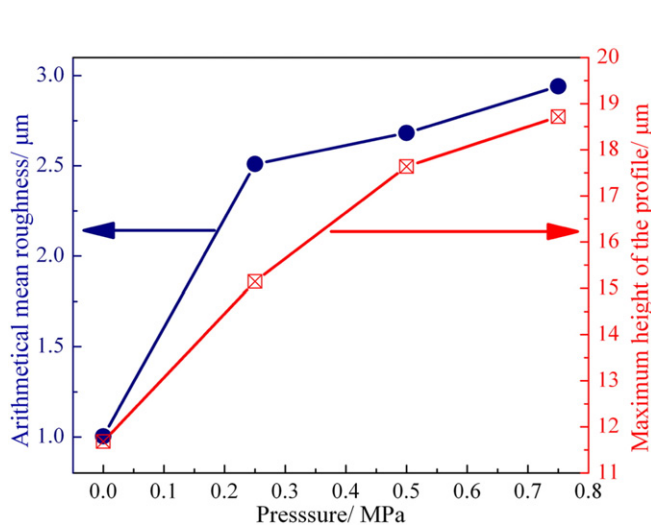


Fig. 4. Results of surface roughness from 3D laser scanning confocal microscopy.

The H^+ ions present in cathodal sample surface combine with electrons to form atomic hydrogen. Some hydrogen atom is released in the form of hydrogen molecules, whereas others absorb the steel surface and then diffuse into the steel under the role of hydrogen concentration gradient, i.e., high hydrogen concentration in the steel surface region. With increasing SP pressure from 0 MPa (un-SP) to 0.75 MPa, HEI decreases, as shown in Fig. 7, demonstrating that SP improve resistance to reversible hydrogen embrittlement. This is because surface shot peening layer acts as a barrier for hydrogen permeation from the outside into the sample, which can be illustrated from two aspects. On the one hand, hydrogen permeation curves of samples are shown in Fig. 17 and the permeation parameters derived from them are listed in Table 3. It can be observed that un-SP sample is easily permeable to atomic hydrogen, which is proven by the shortest $t_{0.63}$ (2916 s) and the highest D_{app} ($4.43 \times 10^{-11} m^2 s^{-1}$), while value of $t_{0.63}$ becomes longer and value of D_{app} is relatively slower in SP specimens. When SP pressure varies from 0.25 MPa to 0.75 MPa, hydrogen impermeability increases. Furthermore, D_{app} is $2.31 \times 10^{-11} m^2 s^{-1}$, $2.04 \times 10^{-11} m^2 s^{-1}$, $1.89 \times 10^{-11} m^2 s^{-1}$ and $t_{0.63}$ is 5595 s, 6333 s 6838 s for 0.25 MPa, 0.50 MPa, 0.75 MPa SP specimens, respectively. Thus, the amount of permeable hydrogen decreases with an increase

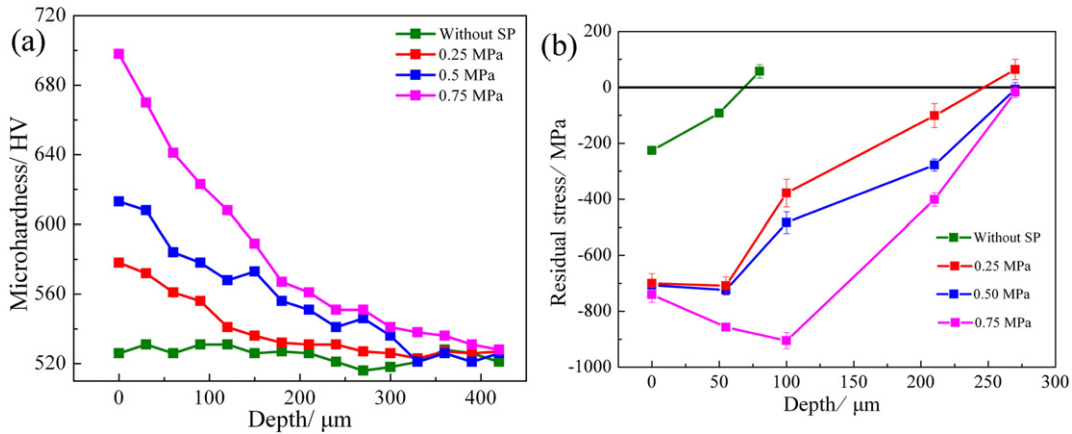


Fig. 5. (a) Microhardness-depth profile; (b) residual stress-depth profile of no shot peening and SP samples.

in SP pressure. On the other hand, fracture surface of hydrogen-charged un-SP specimen shows intergranular and quasi-cleavage fracture mode, as shown in Fig. 10(b), while quasi-cleavage and dimple fracture are observed in 0.75 MPa SP hydrogen-charged specimen, as shown in Fig. 10(d). In fact, it has been established that as the quantity of hydrogen increases, the mode of fracture is changed from dimple to quasi-cleavage and to intergranular fracture [34]. In addition, the onset of intergranular fracture depends on diffusible hydrogen content and higher hydrogen concentration means higher area fraction of intergranular fracture. A study [35] reported that intergranular fracture occurred when diffusible hydrogen content was 0.5 ppm for the 1050 MPa strength level steel and <0.1 ppm for the 1300 MPa strength level steel. Li et al. [11] demonstrated that with increasing hydrogen charging current density from 0.05 mA cm^{-2} to 0.45 mA cm^{-2} , the area fraction

of intergranular fracture monotonously increased. Due to the SP layer prevention from hydrogen invasion, the hydrogen concentration is too low to generate intergranular fracture.

As mentioned above, SP layers play the key role in suppressing hydrogen invasion into specimens and HEI decreases with increasing SP pressure. Actually, this is ascribed to three reasons. 1) The relatively low cathodal hydrogen charging current density in SP samples. It has been reported that the hydrogen concentration in steel increases with increasing hydrogen charging current density [36,37]. It can be easily noted that with increasing SP pressure surface roughness (both Ra and Rz) increases, as shown in Figs. 3 and 4, that is to say, corresponding surface area is improved. Thus, the practical current density decreases as SP pressure increases. 2) The excellent impermeability owned to increasing dislocations density. The hydrogen diffusion process is delayed

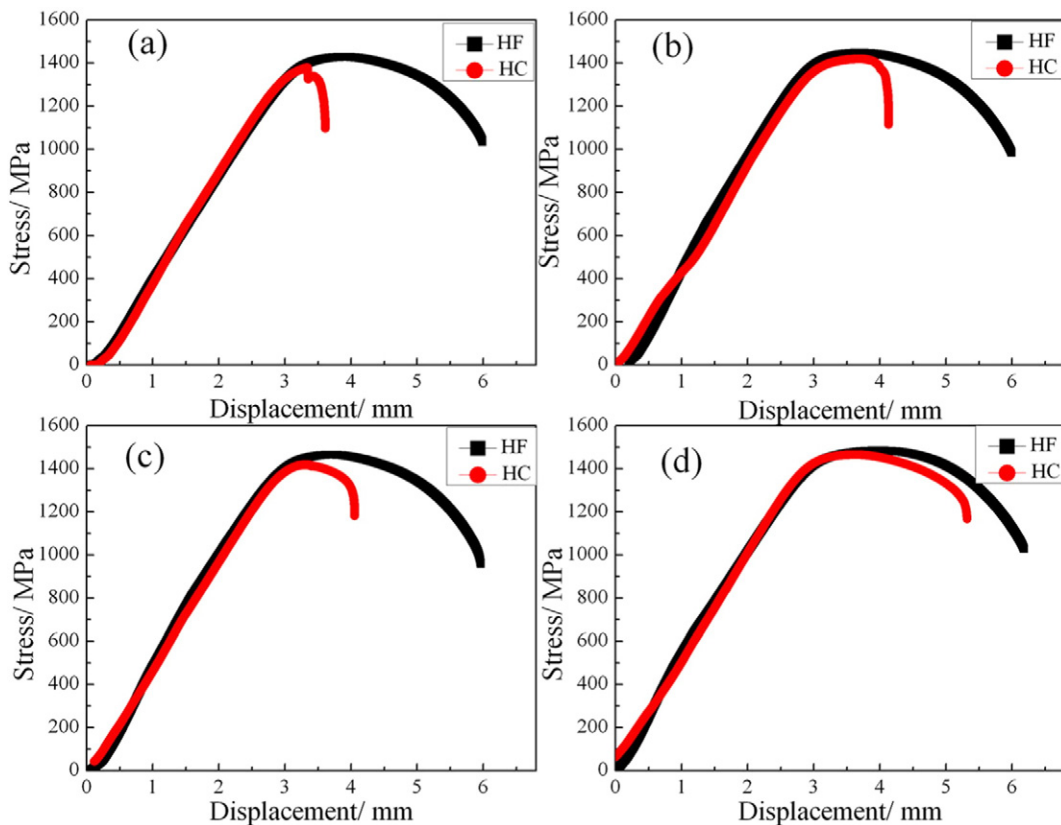


Fig. 6. Stress-displacement curves for hydrogen-free (HF) and hydrogen-charged (HC) specimens at various SP pressures. (a) No shot peening; (b) 0.25 MPa; (c) 0.50 MPa; (d) 0.75 MPa.

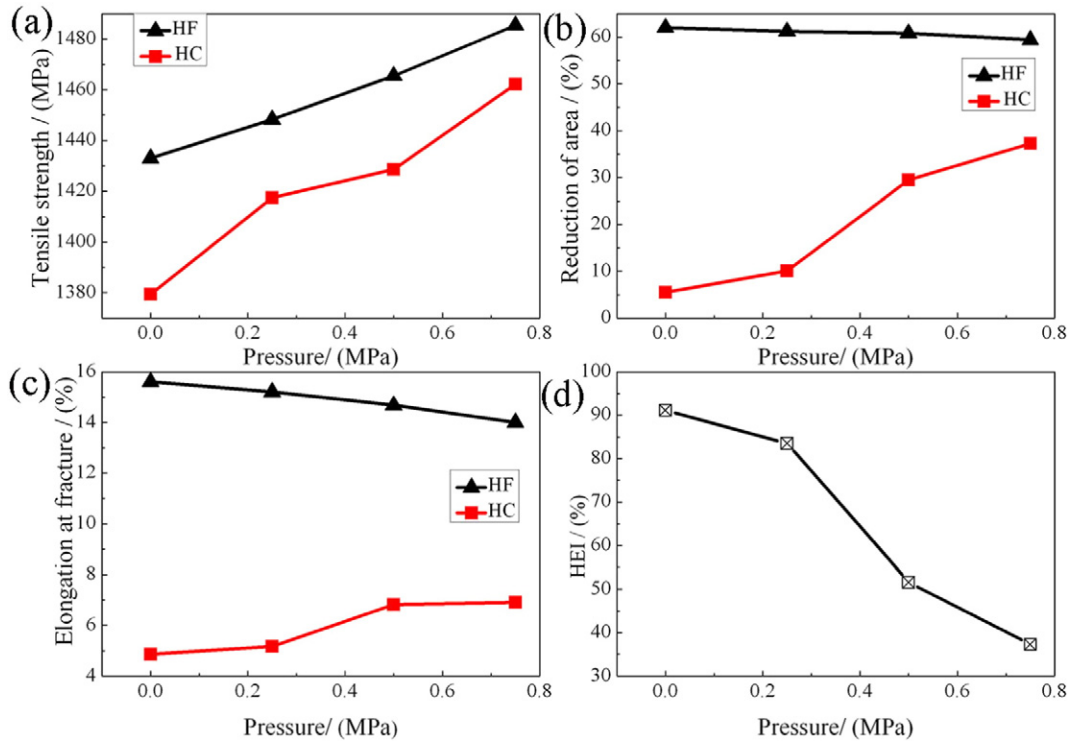


Fig. 7. Mechanical properties for hydrogen-free (HF) and hydrogen-charged (HC) specimens at various SP pressures. (a) Tensile strength; (b) reduction of area; (c) elongation at fracture; (d) HEI.

by the presence of traps, such as vacancies, dislocations, interfaces and microvoids. During hydrogen charging, the hydrogen traps of surface layer are firstly filled with hydrogen and then hydrogen atoms diffuse towards the center of the specimens. It is well-known that the dislocation density in SP layer increases when SP pressure increases [38], as shown in Fig. 2(e) and (f), resulting in the lowest HEI in 0.75 MPa SP sample. 3) The interaction between hydrogen and compressive residual stress. The hydrostatic stress, which affects significantly the hydrogen diffusion and enrichment, at the surface is associated with the residual stress. Compressive residual stress reduces both hydrostatic stress and lattice spacing, and then suppresses hydrogen invasion. Takakuwa et al. [39] revealed that hydrogen concentration around the crack tip increased with tensile stress and was suppressed by compressive residual stress. With residual stresses of -500 MPa, 0 MPa, and 500 MPa, the maximum hydrogen concentration normalized by the external concentration were 1.00 , 1.75 and 5.17 , respectively. The macroscopic

compressive residual stress is generated after SP and the maximum value of compressive stress increases with SP pressure, as shown in Fig. 5, causing a decrease in HEI with increasing SP pressure.

4.2. Effect of SP treatment on irreversible hydrogen embrittlement

HIC is highly dependent on inclusions, which serve as crack initiation sites. Elboudaini and Revie [40] demonstrated that the elongated MnS inclusions were primarily responsible for HIC. With a decrease in volume fraction and total length of inclusions, the resistance to HIC increased. Thus, it is suggested that moderate Ca additions improved HIC resistance through sulfide inclusions shape control by breaking up the normally elongated inclusions to a more spherical shape [41]. Huang et al. [33] reported that most of the HIC cracks initiated from the inclusions rich in Mn, Al, Ca and Ti, while no cracks were observed at inclusions rich in Si, which was due to the fact that this type inclusions can be easily deformed, relieving effectively the residual stress. Moreover, the spherical inclusions were relatively small local lattice deflection with matrix. However, Jin et al. [37] found that the cracks were primarily associated with the Al- and Si-enriched inclusions, rather than the elongated MnS inclusion. The present study reveals that HIC initiates from the inclusions rich in O, Fe, Al and Si or in O, Fe, Si and S for un-SP samples (Fig. 14), while in the SP samples the cracks initiation are associated with both oxide inclusions rich in Si (Fig. 15(a)) and crater rims (Fig. 15(c)). It is reported [5,11,37] that inclusions rich in Al and Si are hard, brittle and incoherent with the metal matrix. The interfaces between matrix and inclusions are regarded as irreversible hydrogen traps. During hydrogen charging, hydrogen atoms diffuse preferentially towards these defects, accumulate and then form hydrogen pressure through the reaction ($2H^+ \rightarrow H_2(gas)$), leading to interfacial decohesion and crack nucleation. Subsequently, by connecting adjacent cracks caused by the formation of hydrogen pressure, crack propagation exhibits stepwise crack features, as shown in Fig. 15(e). It is worth noting that the crack origin is located along the crater rims (as indicated by red ellipses in Fig. 11 and by black arrow in Fig. 14(c) and (d)) and some cracks grow along the crater rims (Fig. 15(d)) in SP samples. On

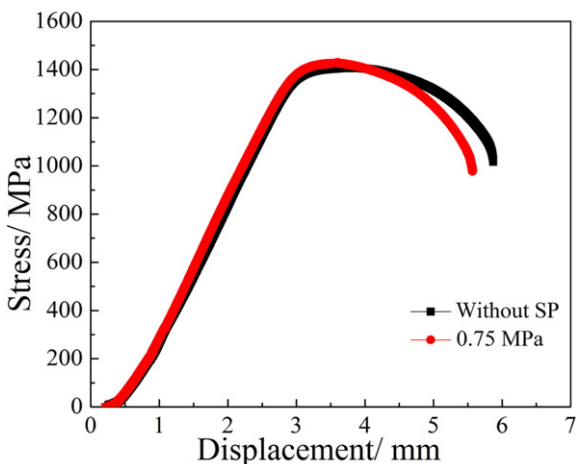


Fig. 8. Stress-displacement curves of hydrogen-charged samples tempered at 200 $^{\circ}C$ for 1 h.

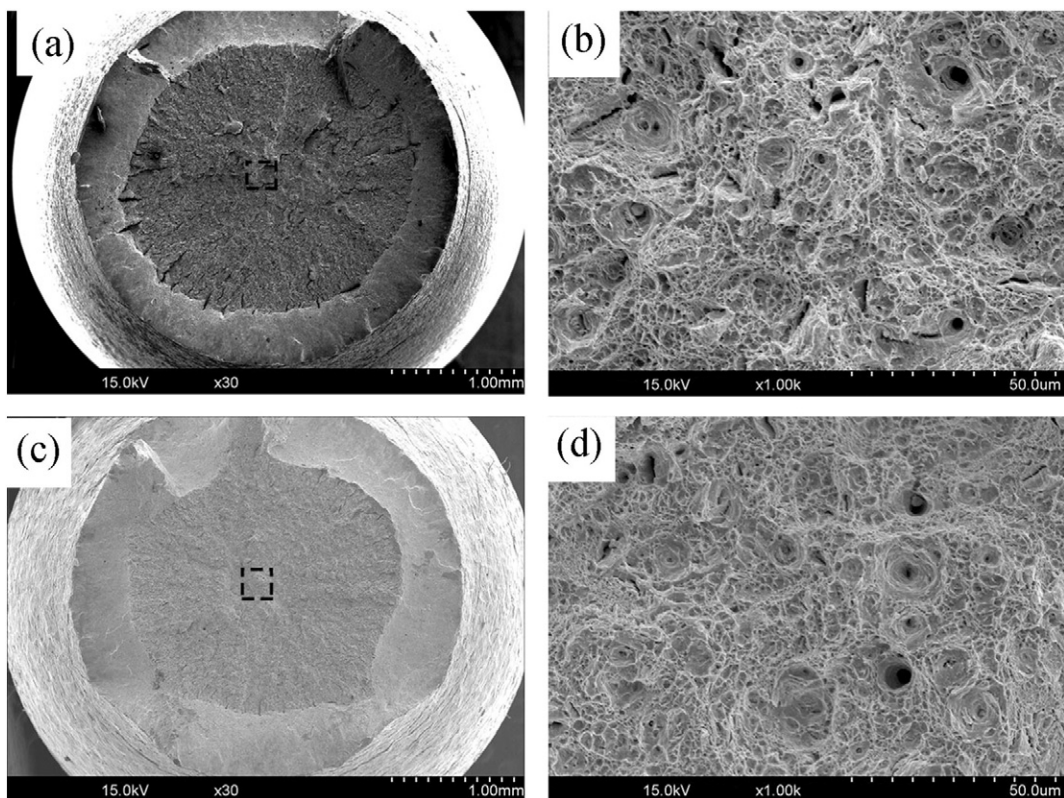


Fig. 9. SEM fractographs of hydrogen-free specimens. (a) Macro-fracture appearance of no shot peening specimen; (b) high magnification image of the signified region in image (a); (c) macro-fracture appearance of SP specimen (0.75 MPa); (d) high magnification image of the signified region in image (c).

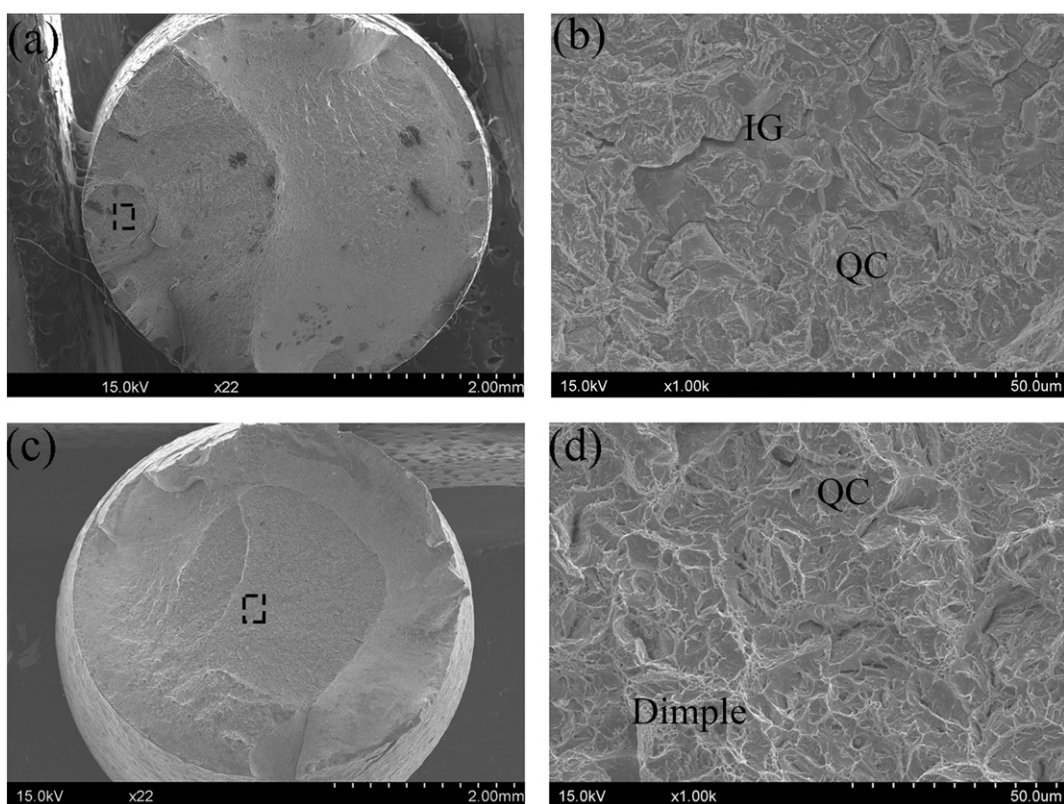


Fig. 10. SEM fractographs of hydrogen-charged specimens. (a) Macro-fracture appearance of no shot peening specimen; (b) high magnification image of the signified region in image (a); (c) macro-fracture appearance of SP specimen (0.75 MPa); (d) high magnification image of the signified region in image (c). IG: intergranular fracture. QC: quasi-cleavage fracture.

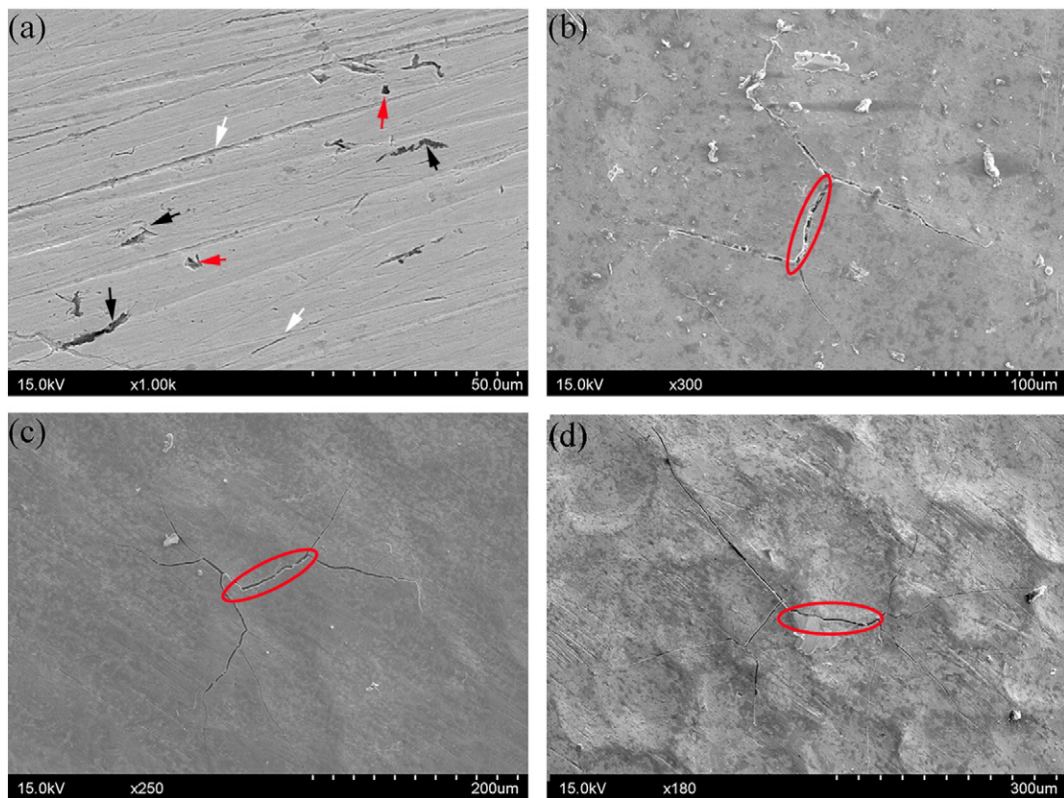


Fig. 11. SEM images showing overviews of hydrogen-induced cracks at different SP pressures. (a) No shot peening; (b) 0.25 MPa; (c) 0.50 MPa; (d) 0.75 MPa. Black arrows indicate long strip shape crack. Red arrows show the circle crack. White arrows indicate remaining mechanical polishing scratches. Red ellipses show the specific crack along the crater rims.

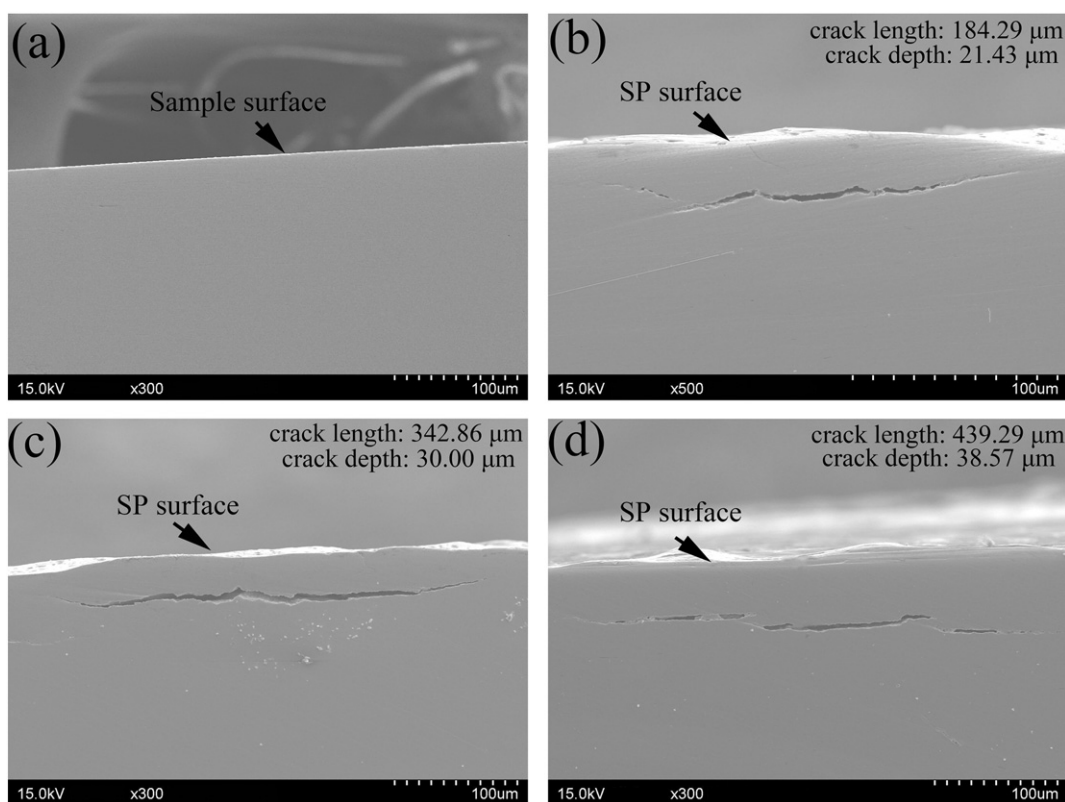


Fig. 12. SEM images showing HIC maximum crack along transversal section at various SP pressures. (a) No shot peening; (b) 0.25 MPa; (c) 0.50 MPa; (d) 0.75 MPa.

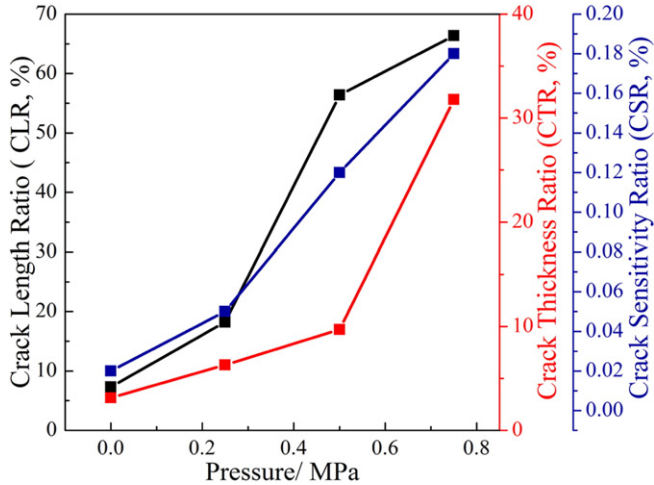


Fig. 13. HIC parameters of samples at various SP pressures.

the one hand, the resistance to HIC is related with microstructure. It has been reported that the regions with minimum microhardness, such as softened heat-affected zone, were observed to become a preferential site for crack nucleation. Additionally, soft regions provided plastic zones, through which the existing blisters were prone to link to each other [8,42]. Kim et al. [43] also indicated that the soft microstructure was more sensitive to HIC than hard microstructure because of formation of more cracks in steel with soft microstructure in case of steels having the same oxide inclusion level. In comparison with other crater regions, the crater rim is relatively soft due to less plastic deformation. As a consequence, the local lower microhardness in crater rim regions

induces crack origins. On the other hand, residual stress field is introduced after SP treatment, as shown in Fig. 5(b). It can be seen that the macroscopically compressive residual stress, which is the average value of area $1 \times 1 \text{ mm}^2$ (the X-ray spot size), increases with increasing SP pressure at the same depth from the surface. However, we should pay much more attention to the local residual stress state of single crater, such as stress at the crater rim and at crater floor, for SP samples hydrogen-induced crack. Unfortunately, the minimum X-ray spot size $1 \times 1 \text{ mm}^2$ is estimated to interrogate at least 80 shot peening craters simultaneously with the average diameter of a crater about $125 \mu\text{m}$. Thus, it is impossible to determine the residual stress state of a crater on the basis of present experiment method. Thankfully, with the aid of numerical simulations, Mahmoudi et al. [44] studied the distribution of residual stress after multi-impact SP treatment and revealed the crater rim region exhibited tensile stress state, as shown in Fig. 18. Boyce et al. [45] assessed the residual stress state caused by a spherical projectile impacting upon a flat surface, suggesting that a small but intense region at the surface immediately outside the crater rim was tensile region and the maximum value of tensile stress was found to be approximately 40% of nominal yield stress while the substantial compressive stress was formed in the crater floor region. Locally tensile residual surface stress could act as a site for crack formation, leading to a degradation in the fatigue life, as reported by Wohlfahrt [46] and Peters [47]. In comparison with compressive stress, tensile stress leads to an increase in the lattice spacing, facilitating hydrogen diffusion and accumulation. Hence, the HIC initiates from the crater rim.

With increasing SP pressure, the susceptibility to HIC increases, as shown in Fig. 13, which is consistent with the references [21–23]. But these researches had focused on the peening effect on reversible hydrogen embrittlement rather than irreversible hydrogen embrittlement. On the one hand, on the basis of Fick's law, hydrogen concentration

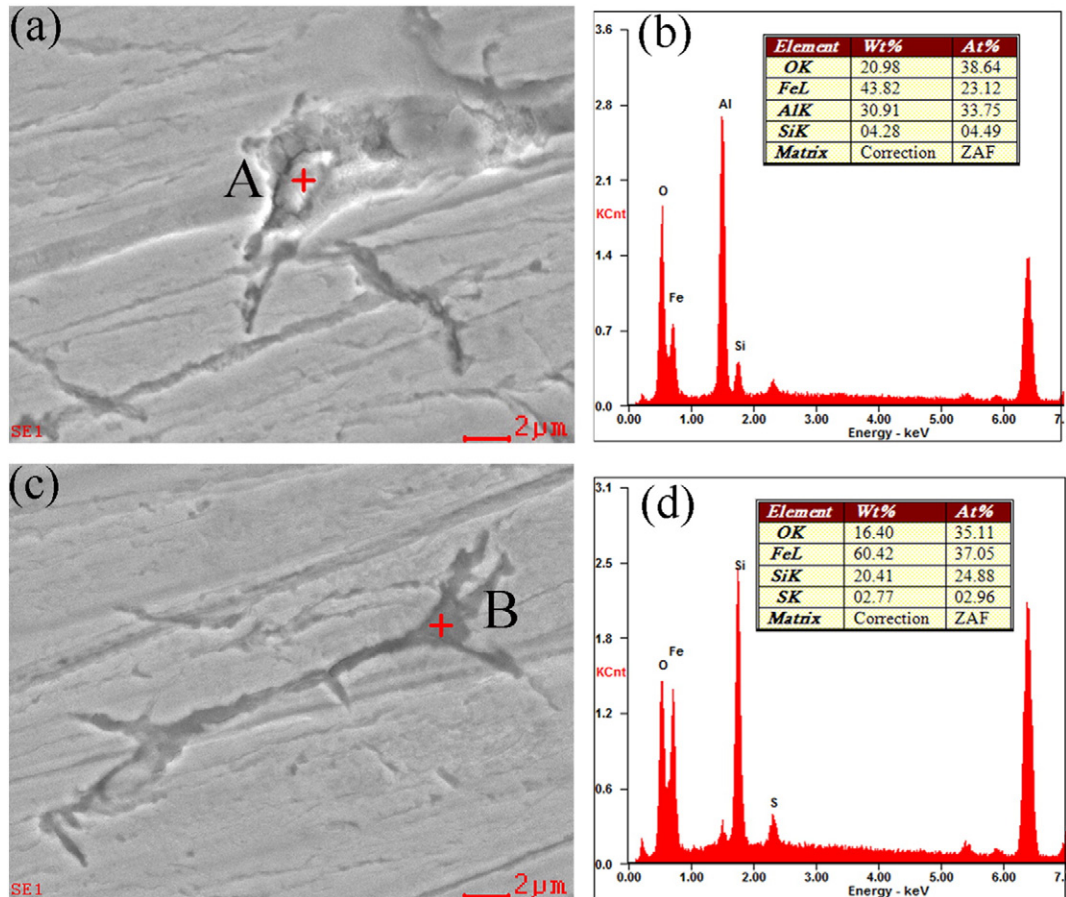


Fig. 14. SEM images showing HIC crack initiation in no shot peening sample. (a) and (c) crack initiation at the inclusions, EDS on the inclusion A (b) and B (d).

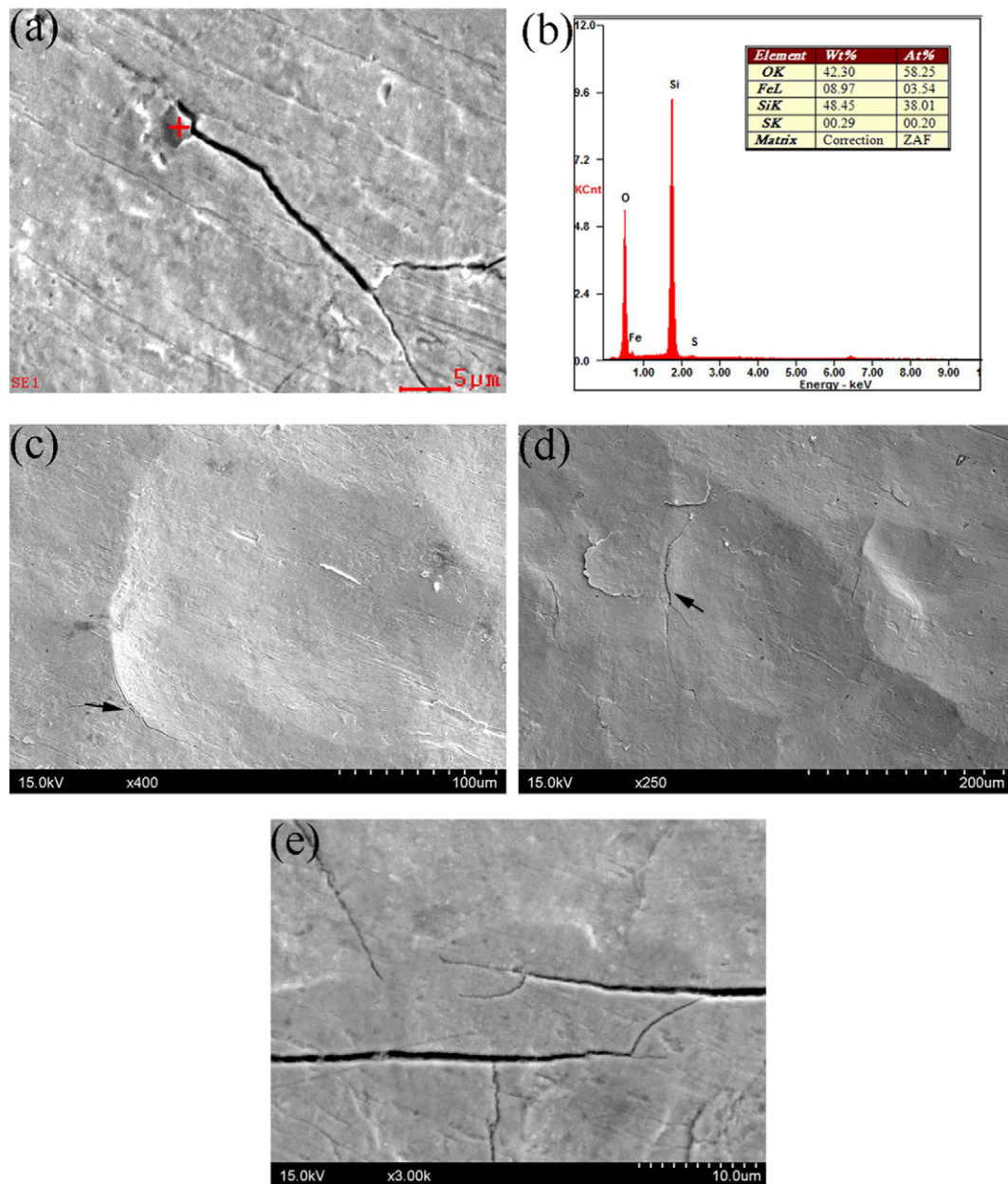


Fig. 15. SEM images showing HIC crack initiation in SP sample (0.75 MPa). (a) Crack initiation at the inclusion; (b) EDS on the inclusion; (c) crack initiation at the rim of craters; (d) crack propagation along the crater rim; (e) stepwise cracks propagation. Black arrows show the crack.

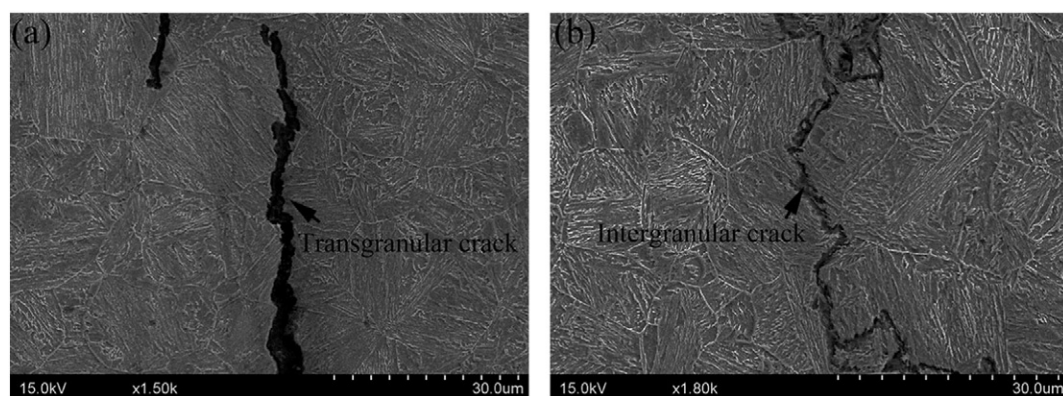


Fig. 16. Crack propagation path beneath the shot peening layer for 0.75 MPa SP sample subjected to HIC test. (a) Transgranular crack (b) intergranular crack.

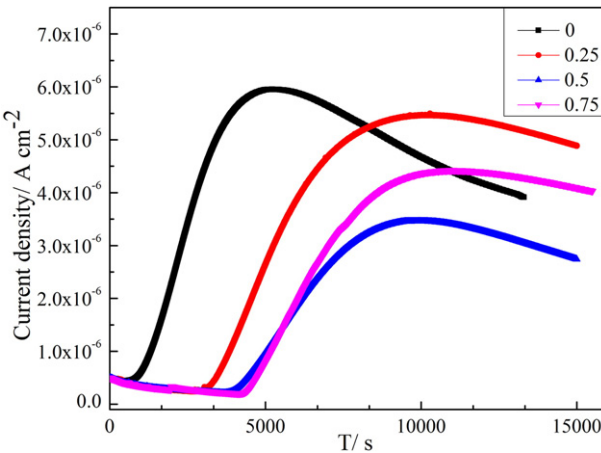


Fig. 17. Hydrogen permeation curves of no shot peening and SP samples.

distribution in the specimens along the radial direction during the hydrogen-charged test can be expressed as:

$$C(x, t) = C_0 + (C_S - C_0) \left[1 - \operatorname{erf} \left(\frac{x}{2\sqrt{Dt}} \right) \right] \quad (10)$$

where x is the depth from the specimen surface, C_0 is the initial hydrogen concentration in the specimen, C_S is the hydrogen concentration at the specimen surface during the charging, D is the diffusion coefficient of hydrogen, t is the charging time. It is evident that when $\frac{x}{2\sqrt{Dt}} \geq 2$, $C \rightarrow 0$. Thus, the maximum hydrogen penetration depth x_{\max} at the end of charging can be calculated by taking $\frac{x_{\max}}{2\sqrt{Dt}} = 2$, i.e. $x_{\max} = 4\sqrt{Dt}$. Drawing the numbers hydrogen diffusion coefficient of un-SP sample ($4.43 \times 10^{-11} \text{ m}^2 \text{ s}^{-1}$), 0.25 MPa SP sample ($2.31 \times 10^{-11} \text{ m}^2 \text{ s}^{-1}$), 0.50 MPa SP sample ($2.04 \times 10^{-11} \text{ m}^2 \text{ s}^{-1}$) and 0.75 MPa SP sample ($1.98 \times 10^{-11} \text{ m}^2 \text{ s}^{-1}$), and $t = 3600 \text{ s}$, the x_{\max} of hydrogen in specimens can be calculated, i.e. 1.60 mm for un-SP sample, 1.15 mm, 1.08 mm and 1.04 mm for 0.25 MPa, 0.50 MPa and 0.75 MPa SP specimens, respectively. This result implies that the maximum depth of hydrogen permeation decreases with an increase in SP pressure. In addition, hydrogen-induced crack occurs once the hydrogen concentration reaches the critical value. Thus, the area of local hydrogen concentration that is beyond critical value for HIC is more, which is due to less hydrogen permeation, for higher SP pressure, causing higher HIC sensitivity. On the other hand, the stress distribution difference in the crater region is associated with HIC. With increasing SP pressure, the maximum tensile stress at crater rim region increases. A study [45] compared stress predicted by finite element method at two key location in single crater: the center of the crater floor and the crater rim, revealing that the stress at the center of crater floor was -505 MPa and -846 MPa , while stress at crater rim was 267 MPa and 503 MPa for incident velocities 200 m s^{-1} and 300 m s^{-1} respectively. Wang et al. [48] revealed that compressive residual stress was obtained within the laser shot, whereas the tensile residual stress was predicted out of the laser spot. The maximum tensile residual stress increased as the laser power density enhanced. Local higher tensile stress at crater rim in higher SP pressure,

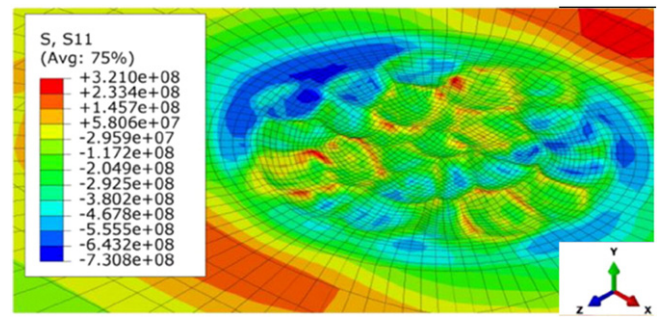


Fig. 18. Distribution of residual stress by shot peening in grinding sample [44].

which promotes crack formation and propagation, causes lower resistance to HIC.

5. Conclusion

In this study, the effect of shot peening treatment on reversible and irreversible hydrogen embrittlement of PSB1080 steel was investigated using slow strain rate tensile tests and electrochemical hydrogen charging-induced cracking tests, respectively. The following conclusions can be drawn.

- (1) With increasing in SP pressure, the hydrogen diffusion coefficient gradually decreases. The value of apparent hydrogen diffusivity is $4.43 \times 10^{-11} \text{ m}^2 \text{ s}^{-1}$ for un-SP sample, and $2.31 \times 10^{-11} \text{ m}^2 \text{ s}^{-1}$, $2.04 \times 10^{-11} \text{ m}^2 \text{ s}^{-1}$, $1.89 \times 10^{-11} \text{ m}^2 \text{ s}^{-1}$ for 0.25 MPa, 0.50 MPa, 0.75 MPa SP sample, respectively.
- (2) For SSRT tests, the resistance to hydrogen embrittlement increases as the SP pressure increases. The surface shot peening layer serves as a barrier from hydrogen invasion, which can be explained from three aspects: the relatively low cathodal hydrogen charging current density in SP samples, the excellent impermeability owned to increasing dislocations density and the interaction between hydrogen and macroscopically residual compression stress.
- (3) Intergranular and quasi-cleavage fracture are observed in un-SP sample, while SP specimen shows quasi-cleavage with some dimple fracture mode, implying that SP treatment delays the onset of intergranular fracture.
- (4) For HIC tests, the resistance to HIC decreases as SP pressure increases. This is related with low hydrogen permeation behaviors and local high tensile stress at crater rim.
- (5) The HIC crack initiates from inclusions rich in O, Fe, Al and Si or in O, Fe, Si and S for un-SP sample, while for SP specimen both inclusions and crater rim serve as crack origins. In addition, SP treatment leads to a crack path transition from a long strip shape in un-SP sample to the branch-type cracks in SP specimens.

Acknowledgments

This research was financially supported by the Doctoral Research Assistant Foundation of Xi'an Jiaotong University.

References

- [1] R.M. Schroeder, I.L. Müller, Stress corrosion cracking and hydrogen embrittlement susceptibility of an eutectoid steel employed in prestressed concrete, *Corros. Sci.* 45 (2003) 1969–1983.
- [2] S. Das, J. Mathur, T. Bhattacharyya, S. Bhattacharyya, Failure analysis of re-bars during bending operations, *Case Stud. Eng. Fail. Anal.* 2 (2014) 51–53.
- [3] F.J. Recio, Y. Wu, M.C. Alonso, U. Nürnberger, Hydrogen embrittlement risk in cold-drawn stainless steels, *Mater. Sci. Eng. A* 564 (2013) 57–64.
- [4] G.E. Monfore, G.J. Verbeck, Corrosion of prestressed wire in concrete, *ACI Struct. J.* (1900).

Table 3
Experimental hydrogen permeability data.

Treatment (MPa)	$t_{0.63}$ (s)	J_∞ (mol m ⁻² s ⁻¹)	D_{app} (m ² s ⁻¹)	C_{app} (mol m ⁻³)
0	2916	6.15×10^{-7}	4.43×10^{-11}	12.21
0.25	5595	5.63×10^{-7}	2.31×10^{-11}	21.44
0.5	6333	3.59×10^{-7}	2.04×10^{-11}	15.48
0.75	6838	4.57×10^{-7}	1.89×10^{-11}	21.27

- [5] X. Li, J. Zhang, P. Zhang, P. Li, X. Song, Failure analysis of high strength steel bar used in a wind turbine foundation, *J. Fail. Anal. Prev.* 15 (2015) 295–299.
- [6] I.I. Vasilenko, G.V. Karpenko, S.I. Mikitishin, N.N. Tkachenko, Reversible and irreversible hydrogen embrittlement, *Sov. Mater. Sci.* 1 (1966) 430–431.
- [7] R.A. Carneiro, R.C. Ratnapuli, V.D.F.C. Lins, The influence of chemical composition and microstructure of API linepipe steels on hydrogen induced cracking and sulfide stress corrosion cracking, *Mater. Sci. Eng. A* 357 (2003) 104–110.
- [8] C.R.F. Azevedo, Failure analysis of a crude oil pipeline, *Eng. Fail. Anal.* 14 (2007) 978–994.
- [9] B.A. Szost, R.H. Vegter, P.E.J. Rivera-Díaz-del-Castillo, Developing bearing steels combining hydrogen resistance and improved hardness, *Mater. Des.* 43 (2013) 499–506.
- [10] X. Li, J. Zhang, Y. Wang, S. Shen, X. Song, Effect of hydrogen on tensile properties and fracture behavior of PH 13–8 Mo steel, *Mater. Des.* 108 (2016) 608–617.
- [11] X. Li, J. Zhang, Y. Wang, B. Li, P. Zhang, X. Song, Effect of cathodic hydrogen-charging current density on mechanical properties of prestrained high strength steels, *Mater. Sci. Eng. A* 641 (2015) 45–53.
- [12] A. Griesche, E. Dabah, T. Kannengiesser, N. Kardjilov, A. Hilger, I. Manke, Three-dimensional imaging of hydrogen blister in iron with neutron tomography, *Acta Mater.* 78 (2014) 14–22.
- [13] Y. Sun, H. Fujii, H. Imai, K. Kondoh, Suppression of hydrogen-induced damage in friction stir welded low carbon steel joints, *Corros. Sci.* 94 (2015) 88–98.
- [14] Y. Lv, L. Lei, L. Sun, Influence of different combined severe shot peening and laser surface melting treatments on the fatigue performance of 20CrMnTi steel gear, *Mater. Sci. Eng. A* 658 (2016) 77–85.
- [15] J.Z. Lu, H. Qi, K.Y. Luo, M. Luo, X.N. Cheng, Corrosion behaviour of AISI 304 stainless steel subjected to massive laser shock peening impacts with different pulse energies, *Corros. Sci.* 80 (2014) 53–59.
- [16] P. Peyre, X. Scherpereel, L. Berthe, C. Carboni, R. Fabbro, G. Béranger, et al., Surface modifications induced in 316L steel by laser peening and shot-peening. Influence on pitting corrosion resistance, *Mater. Sci. Eng. A* 280 (2000) 294–302.
- [17] J.O.M. Bogkris, W. Beck, M.A. Genshaw, P.K. Subramanyan, F.S. Williams, The effect of stress on the chemical potential of hydrogen in iron and steel, *Acta Metall.* 19 (1971) 1209–1218.
- [18] B.E. Wilde, T. Shimada, Surface modification: a potential new approach to combating hydrogen induced fracture in steel, *Scr. Metall.* 22 (1988) 551–556.
- [19] C.L. Ma, T. Takasugi, S. Hanada, Suppression of environmental embrittlement of Ni₃(Si,Ti) alloys by shot peening, *Scr. Mater.* 34 (1996).
- [20] O. Takakuwa, H. Soyama, Suppression of hydrogen-assisted fatigue crack growth in austenitic stainless steel by cavitation peening, *Int. J. Hydrog. Energy* 37 (2012) 5268–5276.
- [21] C. Verpoort, D.J. Duquette, N.S. Stoloff, A. Neu, The influence of plastic deformation on the hydrogen embrittlement of nickel, *Mater. Sci. Eng.* 64 (1984) 135–145.
- [22] A.M. Brass, J. Chêne, G. Anteri, J. Ovejero-Garcia, L. Castex, Role of shot-peening on hydrogen embrittlement of a low-carbon steel and a 304 stainless steel, *J. Mater. Sci.* 26 (1991) 4517–4526.
- [23] C.S. Marchi, T. Zaleski, S. Lee, N.Y.C. Yang, B. Stuart, Effect of laser peening on the hydrogen compatibility of corrosion-resistant nickel alloy, *Scr. Mater.* 58 (2008) 782–785.
- [24] D. Levchuk, F. Koch, H. Maier, H. Bolt, Deuterium permeation through Eurofer and α -alumina coated Eurofer, *J. Nucl. Mater.* 328 (2004) 103–106.
- [25] K. Saito, S. Inayoshi, Y. Ikeda, Y. Yang, S. Tsukahara, TiN thin film on stainless steel for extremely high vacuum material, *J. Vac. Sci. Technol. A* 10 (1995) 556–561.
- [26] F. Reiter, S. Tominetti, A. Perújo, Tritium transport in the water cooled Pb-17Li blanket concept of DEMO, *Fusion Eng. Des.* 15 (1991) 223–234.
- [27] I.C. Noyan, J.B. Cohen, *Residual Stress : Measurement by Diffraction and Interpretation*, Springer, 1987.
- [28] N. Winzer, O. Rott, R. Thiessen, I. Thomas, K. Mraczek, T. Höche, et al., Hydrogen diffusion and trapping in Ti-modified advanced high strength steels, *Mater. Des.* 92 (2016) 450–461.
- [29] X. Li, Y. Wang, P. Zhang, B. Li, X. Song, J. Chen, Effect of pre-strain on hydrogen embrittlement of high strength steels, *Mater. Sci. Eng. A* 616 (2014) 116–122.
- [30] P. Zhang, J. Lindemann, C. Leyens, Shot peening on the high-strength wrought magnesium alloy AZ80—effect of peening media, *J. Mater. Process. Technol.* 210 (2010) 445–450.
- [31] F. Huang, X.G. Li, J. Liu, Y.M. Qu, C.W. Du, Effects of alloying elements, microstructure, and inclusions on hydrogen induced cracking of $\times 120$ pipeline steel in wet H 2 S sour environment, *Mater. Corros.* 63 (2012) 59–66.
- [32] B. Beidokhti, A. Dolati, A.H. Koukabi, Effects of alloying elements and microstructure on the susceptibility of the welded HSLA steel to hydrogen-induced cracking and sulfide stress cracking, *Mater. Sci. Eng. A* 507 (2009) 167–173.
- [33] F. Huang, X.G. Li, J. Liu, Y.M. Qu, J. Jia, C.W. Du, Hydrogen-induced cracking susceptibility and hydrogen trapping efficiency of different microstructure $\times 80$ pipeline steel, *J. Mater. Sci.* 46 (2011) 715–722.
- [34] W. Shen, Characteristic of hydrogen embrittlement (HE) in OCr13Ni4Mo steel and estimate of the safety of cast giant vane of hydraulic turbine for HE, *Foundry* (1985).
- [35] M. Wang, E. Akiyama, K. Tsuzaki, Hydrogen degradation of a boron-bearing steel with 1050 and 1300 MPa strength levels, *Scr. Mater.* 52 (2005) 403–408.
- [36] C.F. Dong, K. Xiao, Z.Y. Liu, W.J. Yang, X.G. Li, Hydrogen induced cracking of $\times 80$ pipeline steel, *Int. J. Miner. Metall. Mater.* 17 (2010) 579–586.
- [37] T.Y. Jin, Z.Y. Liu, Y.F. Cheng, Effect of non-metallic inclusions on hydrogen-induced cracking of API5L $\times 100$ steel, *Int. J. Hydrot. Energy* 35 (2010) 8014–8021.
- [38] Q. Feng, C. Jiang, Z. Xu, L. Xie, V. Ji, Effect of shot peening on the residual stress and microstructure of duplex stainless steel, *Surf. Coat. Technol.* 226 (2013) 140–144.
- [39] O. Takakuwa, M. Nishikawa, H. Soyama, Numerical simulation of the effects of residual stress on the concentration of hydrogen around a crack tip, *Surf. Coat. Technol.* 206 (2012) 2892–2898.
- [40] M. Elboudaini, R.W. Revie, Metallurgical factors in stress corrosion cracking (SCC) and hydrogen-induced cracking (HIC), *J. Solid State Electrochem.* 13 (2009) 1091–1099.
- [41] R. Kane, M. Cayard, Roles of H₂S in the behavior of engineering alloys: a review of literature and experience, *Corrosion* (1998).
- [42] A. Takahashi, H. Ogawa, Influence of microhardness and inclusion on stress oriented hydrogen induced cracking of line pipe steels, *Trans. Iron Steel Inst. Jpn.* 36 (1996) 334–340.
- [43] K.K. Wan, H.G. Jung, G.T. Park, S.U. Koh, K.Y. Kim, Relationship between hydrogen-induced cracking and type I sulfide stress cracking of high-strength linepipe steel, *Scr. Mater.* 62 (2010) 195–198.
- [44] A.H. Mahmoudi, A. Ghasemi, G.H. Farrahi, K. Sherafatnia, A comprehensive experimental and numerical study on redistribution of residual stresses by shot peening, *Mater. Des.* 90 (2016) 478–487.
- [45] B.L. Boyce, X. Chen, J.W. Hutchinson, R.O. Ritchie, The residual stress state due to a spherical hard-body impact, *Mech. Mater.* 33 (2001) 441–454.
- [46] H. Wohlfahrt, *Shot Peening and Residual Stresses*, Springer US, 1981.
- [47] J.O. Peters, R.O. Ritchie, Foreign-object damage and high-cycle fatigue: role of microstructure in Ti-6Al-4V, *Int. J. Fatigue* 23 (2001) 413–421.
- [48] C. Wang, X. Wang, Y. Xu, Z. Gao, Numerical modeling of the confined laser shock peening of the OFHC copper, *Int. J. Mech. Sci.* 108 (2016) 104–114.